Depolymerization Pathways for Branching Lignin Spirodienone Units Revealed with *ab initio* Steered Molecular Dynamics

Brendan D. Mar[1] and Heather J. Kulik[1,*]

[1]*Department of Chemical Engineering, Massachusetts Institute of Technology, Cambridge, MA 02139*

ABSTRACT: Lignocellulosic biomass is an abundant, rich source of aromatic compounds, but direct utilization of raw lignin has been hampered by both the high heterogeneity and variability of linking bonds in this biopolymer. *Ab initio* steered molecular dynamics (AISMD) has emerged both as a fruitful direct computational screening approach to identify products that occur through mechanical depolymerization (i.e., in sonication or ball-milling) and as a sampling approach. By varying the direction of force and sampling over 750 AISMD trajectories, we identify numerous possible pathways through which lignin depolymerization may occur in pyrolysis or through catalytic depolymerization as well. Here, we present eight unique major depolymerization pathways discovered via AISMD for the recently characterized spirodienone lignin branching-linkage that may comprise around 10% weight of all lignin in some softwoods. We extract representative trajectories from AISMD and carry out reaction pathway analysis to identify energetically favorable pathways for lignin depolymerization. Importantly, we identify dynamical effects that could not be observed through more traditional calculations of bond dissociation energies. Such effects include thermodynamically favorable recovery of aromaticity in the dienone ring that leads to near-barrierless subsequent ether cleavage and hydrogen bonding effects that stabilize newly formed radicals. Some of the most stable spirodienone fragments that reside at most 1 eV above the reactant structure are formed with only 2 eV barriers for C-C bond cleavage, suggesting key targets for catalyst design to drive targeted depolymerization of lignin.

1. Introduction

Lignocellulosic biomass[1-2] has captured much interest in recent years[3-6] as a potential cheap and renewable energy source[7]. Lignin, in particular, is a biopolymer[8] (20-30% of biomass by weight[9]) with high structural heterogeneity that has historically limited its utilization to the fast pyrolysis[10-11] generation of low-grade and volatile bio oil[2] of moderate value[12]. Hydrodeoxygenation or metabolic engineering[3, 13-15] approaches have been pursued to increase the value of these bio oils, but the pyrolysis step alone is energy intensive. Thus, depolymerization of unprocessed lignin remains of significant interest[8, 16] and has been pursued experimentally with polyoxometalate catalysts[17], base-catalyzed hydrolysis[18-19], acidolysis[20-21], ionic liquid treatment[22], reduction with hydrosilanes[23], photochemical degradation[24], and ball milling[25]. In addition to general depolymerization, efforts have also included selective strategies via homogeneous catalysts[26-30] and enzymes[31]. A route to selective depolymerization that both prevents repolymerization and generates a specific set of monomers[32] has only recently had success with the aid of metal catalysts[33-34] capable of producing up to 50% yield.

The natural structural complexity of the lignin biopolymer, which contains eight known linkages between three monomeric units[17], is critical to understanding how to design a catalyst for selective depolymerization starting from raw lignin feedstocks. First-principles simulation can provide valuable insight on the energetics and products of bond cleavage pathways. Previous computational efforts have focused on studying model compounds that contain the abundant β-O-4 ether lignin linkage by evaluating homolytic bond dissociation energies[35-39], mechanical properties[40-43], intramolecular hydrogen bonding[44]. More recently, some kinetic modeling and analysis has been carried out, particularly to model fast pyrolysis[45-50]. Both specific[51] and general

catalysis of lignin depolymerization has been investigated computationally by studying the effect of transition metal catalysts[52-55] and ionic liquids[56-57] on lignin degradation. Few studies[58-59] have focused on the more complex chemistry of the other seven linkages in lignin, despite the fact that β-O-4 may comprise as little as 35% of the lignin linkages, depending upon the feedstock[60].

Inspired in part by recent experimental and computational efforts in efficient mechanistic study of mechanochemical depolymerization[61-67], we recently developed[59] an alternative approach for depolymerization pathway discovery by employing *ab initio* steered molecular dynamics (AISMD). This technique allows us to both directly predict the results of mechanical lignin depolymerization (e.g., by ball milling[25]) and, more importantly, to follow the dynamical processes that occur following bond cleavage beyond what can be observed from homolytic bond dissociation energy (BDE) studies. In our previous work[59], we both surveyed depolymerization dynamics in all eight lignin linkages and identified unusual depolymerization patterns, particularly in branching models. We now follow up on our previous observations[59] of numerous unique depolymerization pathways for the branching spirodienone linkage that was only recently discovered in 2001[68-70]. Spirodienone is now believed to be present in up to 9% (7%) abundance in softwoods (hardwoods)[60], but little is known about the chemistry at this linkage beyond that it readily undergoes ring-opening under acidic conditions[71] as might be applied in pulping[60, 72].

Although the spirodienone linkage has not been the primary focus of computational or mechanistic studies, we anticipate that a firm understanding of pathways for lignin depolymerization at chain branching sites is critical for selective, mild lignin depolymerization. Indeed, the already observed high heterogeneity in possible depolymerization pathways for

spirodienone inspires a follow-up study of the energetics of each pathway to help identify effects not captured by simple calculation of bond dissociation energies. The outline of the rest of this work is as follows. In Sec. 2, we review the details of our computational approach. In Sec. 3, we present and discuss results on the mechanism and energetics of eight major spirodienone depolymerization pathways. Finally, we provide our conclusions in Sec. 4.

2. Computational Details

We carry out all calculations described here with the TeraChem graphical-processing-unit-accelerated quantum chemistry code[73-74]. The AISMD[62] simulations utilize a 0.25 fs timestep with applied force of 4.0 nN from attachment points (APs) to the pulling points (PPs), thus sampling a force-modified potential energy surface (FMPES)[62, 64]. We previously demonstrated[59] an AISMD strategy for discovering both catalyzed and uncatalyzed depolymerization pathways in lignin oligomers with 2-6 repeats. Within AISMD, we define an AP on a molecule at position $\mathbf{r}_i^{\mathrm{AP}}$ and PP at position $\mathbf{r}_i^{\mathrm{PP}}$ towards which the AP is pulled at constant force, F_i. This external (ext) force is defined as:

$$\mathbf{F}_{\mathrm{ext}} = \sum_i^{\mathrm{AP}} F_i \frac{\mathbf{r}_i^{\mathrm{PP}} - \mathbf{r}_i^{\mathrm{AP}}}{\left\| \mathbf{r}_i^{\mathrm{PP}} - \mathbf{r}_i^{\mathrm{AP}} \right\|} \tag{1}$$

and we add this force to the standard ab initio evaluation of the gradient:

$$\mathbf{F}_{\mathrm{total}} = \mathbf{F}_{\mathrm{ab\ initio}} + \mathbf{F}_{\mathrm{ext}} \tag{2}$$

Here, we study a minimal model of the spirodienone linkage that is comprised of 3 p-coumaryl alcohol lignin monomers (Figure 1). All pulling points were placed 90-100 Å away from attachment points, based on the procedure we introduced in our earlier study[59] of lignin

depolymerization to ensure fragments did not run into the PPs after the first cleavage event. An initial temperature of 300 K was set for these runs, but no thermostat was employed during the 400 fs to 2 ps runs. In the brief dynamics time prior to bond cleavage, temperatures remain close to 300 K (i.e., within 50 K), but temperature becomes less meaningful once the fragments are fully separated and their velocities include unrestrained translation to PPs. A total of 300 ps of dynamics over 750 trajectories was obtained from sampling 10 trajectories for each of 75 combinations of two pulling points. The AISMD simulations employed unrestricted hybrid density functional theory (DFT) using the long-range-corrected, ωPBEh exchange-correlation functional (ω=0.2)[75] and the 6-31g basis set. In order to encourage possible convergence to a radical solution, level-shifting (a 1.0 eV shift to open shell states, 0.0 eV on closed shell states)[76] was applied. Qualitative observations are unchanged with alternate semi-local or global hybrid exchange-correlation functional choices (see Supporting Information Table S1).

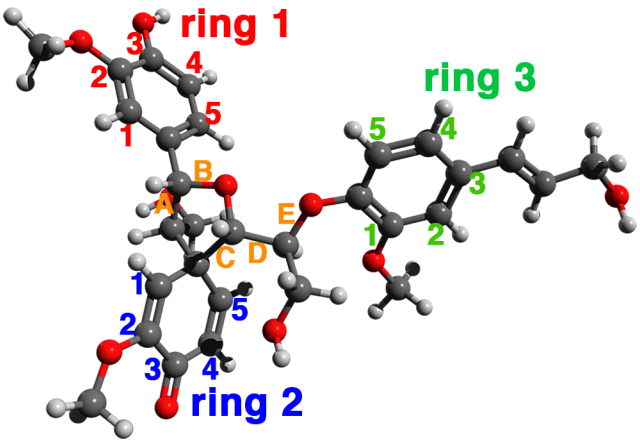

Figure 1. Structure of the spirodienone model used in this work labeled with ring numbers (1 in red, 2 in blue, and 3 in green) and atom indices of APs, which run from 1 through 5 for each ring. The five most frequently cleaved bonds are labeled A-E in orange.

Snapshots were taken from 50 fs past the point in a trajectory at which a new distinct fragment emerged, as defined by a separation distance between nearest atoms from the two fragments being larger than 2.0 Å. For each snapshot, separate fragments were geometry

optimized using DL-FIND[77] with default L-BFGS convergence criteria. Relative energies of these fragments were evaluated with respect to the energy of the original optimized spirodienone model compound. These separated fragments were grouped qualitatively into 8 major fragmentation pathways, as described in the Results and Discussion.

The trajectory that led to the lowest energy set of optimized fragments in each qualitative pathway was selected for further reaction pathway analysis to obtain cleavage barriers and transition states. We employed a modified version of the nebterpolate software[78] to smooth these molecular dynamics trajectories and obtain a good initial guess of the bond breaking event interpolated in internal coordinates. Climbing-image nudged elastic band (NEB) calculations[79-80] were carried out with the DL-FIND[77] optimizer extension to TeraChem for each step in the 8 most abundant pathways identified from AISMD runs using the lowest energy structure obtained in each case. Default spring constants and convergence criteria were employed for the 25 image NEB calculations. We note that this procedure does not guarantee convergence to an exact transition state. However, we treat the highest climbing image in each converged NEB as an approximate transition state (TS) because i) large 74-atom molecule fragments here have numerous soft modes that would make unambiguous vibrational TS characterization challenging, and ii) the reaction steps involve clear bond-cleavage coordinates that we will validate by tracking relevant bond distances (see Sec. 3d).

Partial-charge and bonding analysis was performed using the TeraChem interface to the Natural Bond Orbital (NBO), version 6.0 package[81]. The NBO analysis categorizes transformed orbitals as core, two-center or three-center bonding orbitals, and lone pairs for the generation of Lewis structures. We use the occupancy of each Lewis-like lone pair NBO and natural spin on

each atom to confirm qualitative Lewis structure assignments, especially distinguishing the formation of radicals and diradicals from heterolytic mechanisms.

3. Results and Discussion

3.a. Overview of Spirodienone Cleavage Pathways

Over 750 AISMD trajectories were obtained by varying APs on the spirodienone linkage (Figure 1). For each of the three rings in spirodienone, five APs were defined as atoms within a six membered-ring except for the atom that connected the ring to the rest of the lignin linkage. Two of the rings (ring 1 and ring 3) in spirodienone are aromatic, whereas ring 2 is a dienone. The lack of aromaticity in ring 2 of the spirodienone linkage will play an important role in cleavage pathways discussed shortly. Pairs of APs were chosen from two different rings leading to 75 possible combinations for which 10 trajectories were run. All simulations were carried out at a relatively high, 4.0 nN force, which was designed to ensure that many trajectories lead to cleavage. These forces are likely at the upper end of what is achieved during ball-milling of lignin[25]. Interestingly, no cleavage events were observed between APs on rings 1 and 2, despite the fact that they span an oxygen-containing five-membered ring that should be susceptible to mechanochemical cleavage (near label B in Figure 1) is spanned by the ring 1 to ring 2 AP pairings. Conversely, for APs chosen from rings 2 and 3, 99% of all 250 trajectories sampled led to a cleavage event. In the case of APs chosen from rings 1 and 3, 85% of all 250 trajectories sampled led to a cleavage event (see Supporting Information Tables S2-S4).

Overall, eight major qualitative groupings of cleavage pathways of the spirodienone linkage were observed. Although we previously reported[59] a total of 23 observed pathways for

spirodienone fragmentation, the number reported here is lower because we i) no longer distinguish pathways by the order in which bonds are cleaved and ii) we have discarded late fragmentation events occurring well after the initial separation of the monomers that may have been artifacts due to steered atoms (i.e., the attachment points) arriving at pulling points. In previous work, the AP-PP distances were shorter than in the current data set, and we have increased the initial distance to the PPs, eliminating these spurious pathways.

Despite observing several diverse pathways, all pathways involved the cleavage of only five bonds at the center of the linkage (labeled A-E in Figure 1). Three of the bonds (A-C) are members of the five-membered ring that is positioned between rings 1 and 3 in the linkage, although some bonds such as the C-O bond adjacent to bond C and ring 2 were not observed to cleave. Cleavage of bond E is similar to the β-O-4-like cleavage that has been the frequent focus of previous computational studies[37, 40, 45, 55], whereas most of the remaining bonds have not been characterized previously. Only cleavage at bonds D or E corresponds to single homolytic bond cleavage, whereas the opening of the five-membered ring results in significant rearrangement after formation of a radical. This latter observation is consistent with our earlier studies of the ring-opening in the β-β and β-5 dimers[59]. We thus characterize the eight cleavage pathways in terms of bonds cleaved that lead to a final product distribution.

3.b. Analysis of Dominant Cleavage Pathways and Products

The choice of AP pairs introduces a bias for discovering lignin depolymerization pathways, and we now examine the distribution of each pathway over the various AP pair choices (Figure 2 and Supporting Information Tables S2-S4). Beyond the utility of force-induced depolymerization as a discovery tool, analysis of which portions of the molecule are susceptible

to depolymerization under force has additional benefits. First, it tells us which bonds are mechanochemically most sensitive to degradation (e.g., as evidenced by 100% cleavage through a bond) or most inert (e.g., no cleavage through force applied to a bond). This information is expected to be directly transferable to interpretation of ball-milling depolymerization[25] but should also provide insight following energetic analysis for other conditions (sec. 3.d.). Secondly, analysis of pathway statistics reveals if certain combinations of bonds are most likely to be cleaved together.

The ring 1 (R1) to ring 3 (R3) AP pairs nearly exclusively lead to simple bond cleavage pathways **1** and **2**, which involve homolytic cleavage of a C-C bond, D, or a β-O-4-like bond, E, respectively. The formed products in pathway **1** involve a radical on the tetrahydrofuranal ring and near-monolignol radical containing an extra chain, whereas pathway **2** produces a radical monolignol and leaves the alcohol chain radical attached to the tetrahydrofuranal ring (Figure 3). The transverse AP pairings of R1 AP 1 with R3 APs 2 or 3 are the least productive, leading to only 30% or 20% of breaking in all sampled trajectories, respectively (see Supporting Information Table S3). Almost all other R1 APs (2-5) lead to 100% cleavage, with the R1 AP 2-5 pairings with R3 1-4 leading to 80-100% cleavage through pathway **1** and limited, 0-20% cleavage of the β-O-4-like bond E through pathway **2** (see Supporting Information Table S3).

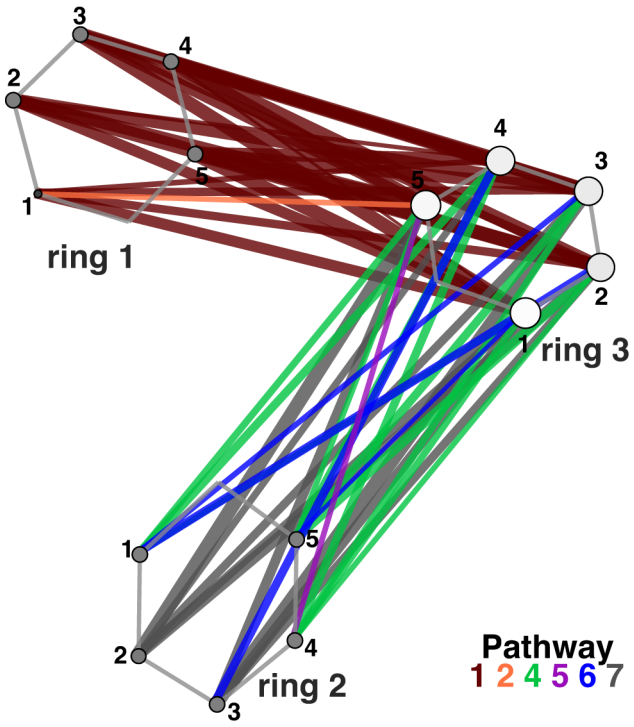

Figure 2. Network graph of dominant breaking pathway (color legend shown in inset) for a given AP pair with thickness of the graph edge corresponding to the number of breaking events (thickest lines indicates 10/10, thinnest lines are 3/10). The total percentage of pathways that break for a simulation involving an atom is indicated by the size and color of the node (near 100% is a large, white circle, and below 50% are the smallest dark circles).

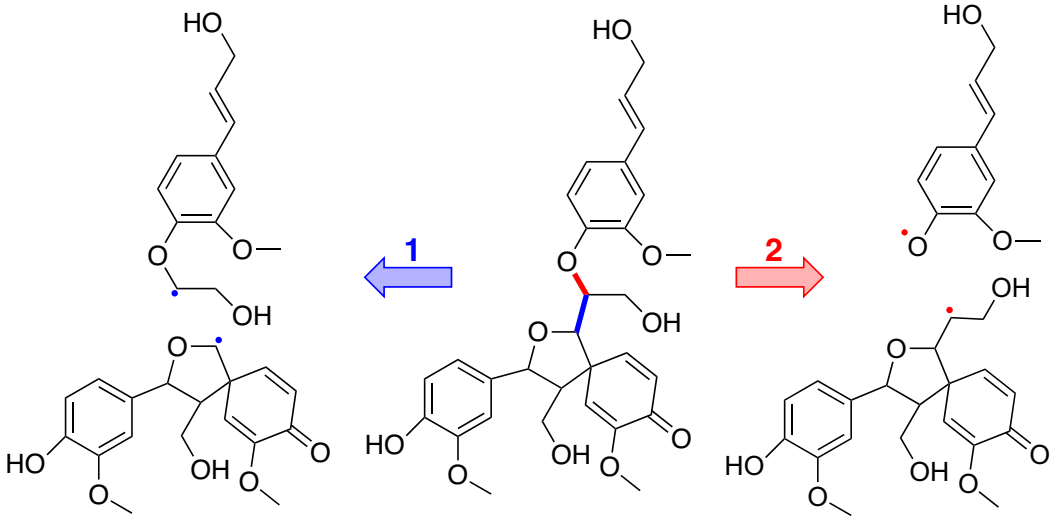

Figure 3. Homolytic bond cleavage pathways **1** (left) and **2** (right) of bonds D (in blue) and E (in red), respectively.

An exception is R3 AP 5, which is closer to the bond E itself and favors in many cases closer to 40% cleavage through pathway **2**. In the R1 AP 1 to R3 AP 5 pair, the pathway **2** cleavage pattern is instead favored with 40% of the cleavage events versus 30% through pathway 1 and 30% leading to no breakage events (Figure 2). Additionally, two R1 AP1 to R3 AP 3 trajectories lead to cleavage pathway **3**, which initiates with homolytic cleavage of bond D but is followed by ring-opening cleavage of bond B, leading to products similar to pathway **1** except with an opened tetrahydrofuranal ring (Supporting Information Figure S1). Overall, the R1-R3 AP pairs primarily lead to relatively similar homolytic cleavage mechanisms that could alternatively be probed via homolytic BDE calculations.

Conversely, a much richer array of rearrangements is observed through combinations of ring 2 (R2) and ring 3 (R3) AP pairs (see Figure 2 and Supporting Information Tables S2 and S4). Nearly all R2 points lead to 100% cleavage, with only R2 AP 4 and R2 AP 2 occasionally yielding unproductive trajectories with R3 AP 2. The R2 AP 2 and R3 AP 2 vectors to their respective PPs can be viewed as nearly parallel, and this may explain the unproductive pulling. Interestingly, although, R2 and R3 are linked by bonds D and E, none of the R2-R3 AP pair bond cleavage trajectories correspond to the simple bond cleavage pathways **1** or **2** of bonds D or E, respectively, nor do they correspond to homolytic D or E cleavage followed by ring opening (Supporting Information Table S4). Instead, all five cleavage pathways (**4**-**8**) observed for these AP combinations initiate through ring-opening cleavage of bond C, which is also oriented in the direction that connects rings 2 and 3. Pathway **4** products are characterized by formation of a monolignol radical and a migrated radical that introduces aromaticity to the dienone ring (Figure 4). This aromaticity may be quantified by comparison of the geometry-optimized aromatic intermediates with the original spirodienone structure. In the original spirodienone structure,

significant differences in bond order are apparent between the short 1.33 Å C-C double bonds with the longer 1.54 Å C-C single bonds. For intermediates where aromaticity is introduced, this > 0.2 Å bond length difference narrows to < 0.05 Å on average with bond lengths in the ring ranging from 1.40 to 1.44 Å.

The dienone ring also becomes aromatic in pathway **5**, but the fragment is a diradical with the isolated functionalized monolignol becoming closed shell (Figure 5). Here, aromaticity may be quantified again by dramatic reduction in bond length alternation in the formerly dienone ring. Both pathways **6** and **7** lead to release of the dienone ring as a closed shell monolignol species, but pathway **6** produces a diradical on the remaining fused lignols, whereas additional fragments are formed in pathway **7** (Figures 6 and 7). Four separate fragments are formed in pathway **8**: a monolignol radical, a hydroxyl radical, and a diradical that rearranges to make the dienone ring aromatic as in pathways **4** and **5** (Supporting Information Figure S2).

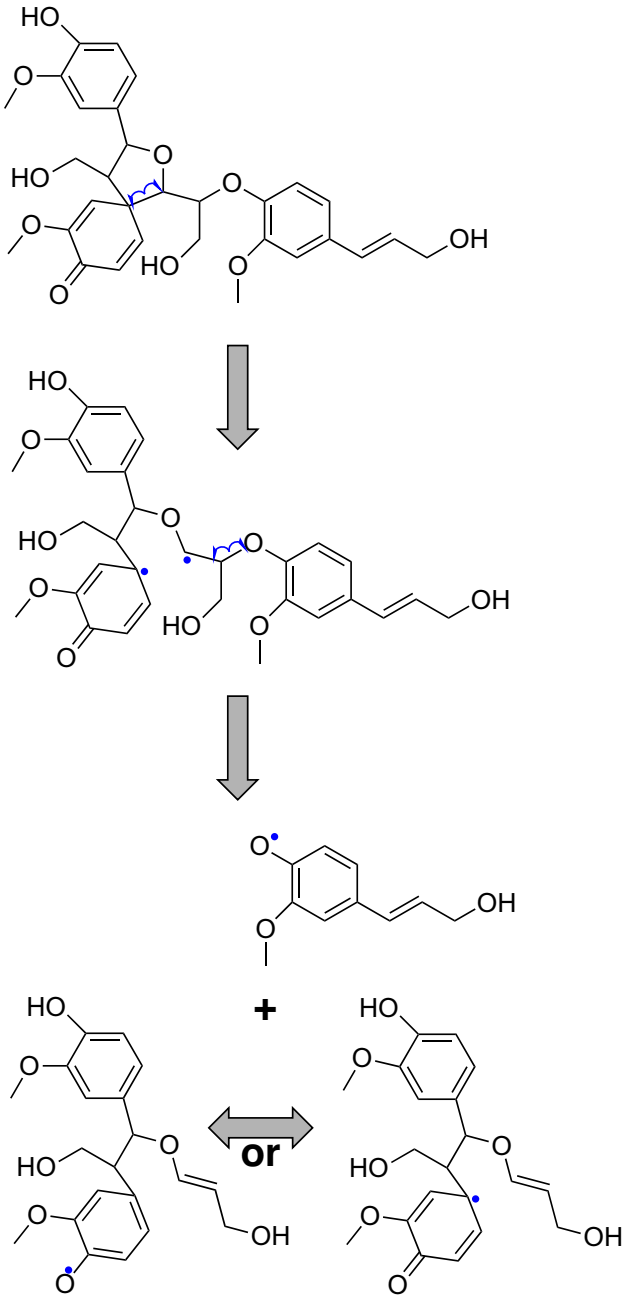

Figure 4. Homolytic bond cleavage pathway **4** with five-membered ring opening of bond C to form a diradical followed by homolytic cleavage of bond E. The radical rearranges on the ring 1-2-derived products in one case to form a new aromatic ring.

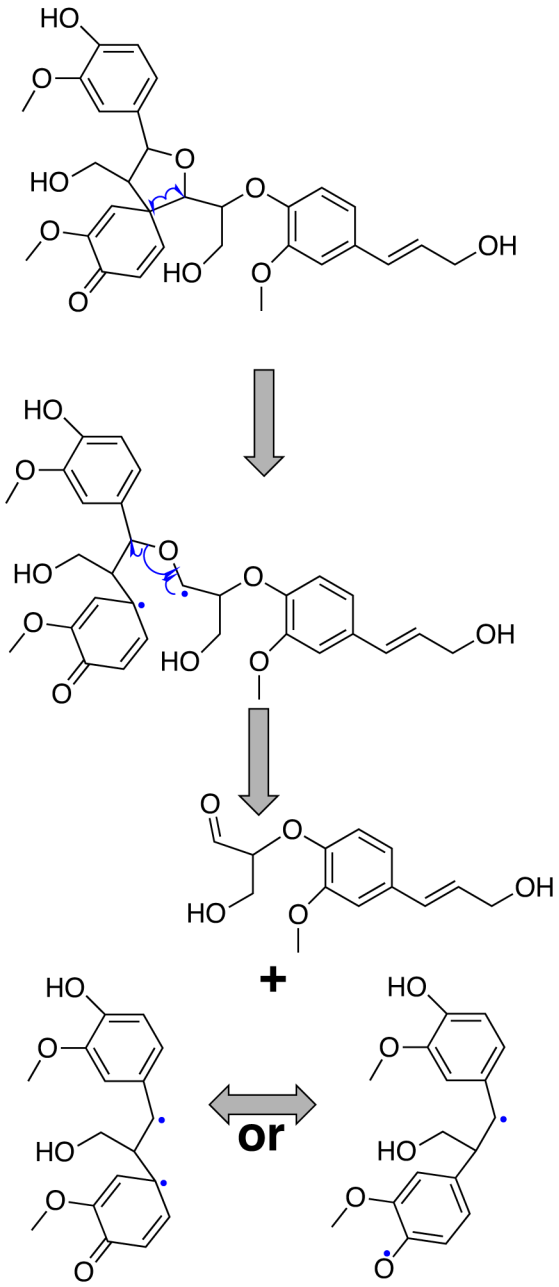

Figure 5. Homolytic bond cleavage pathway **5** with five-membered ring opening of bond C to form a diradical followed by homolytic cleavage of bond B. The diradical rearranges on the ring 1-2-derived products in two ways, in one case introducing aromatic character to ring 2.

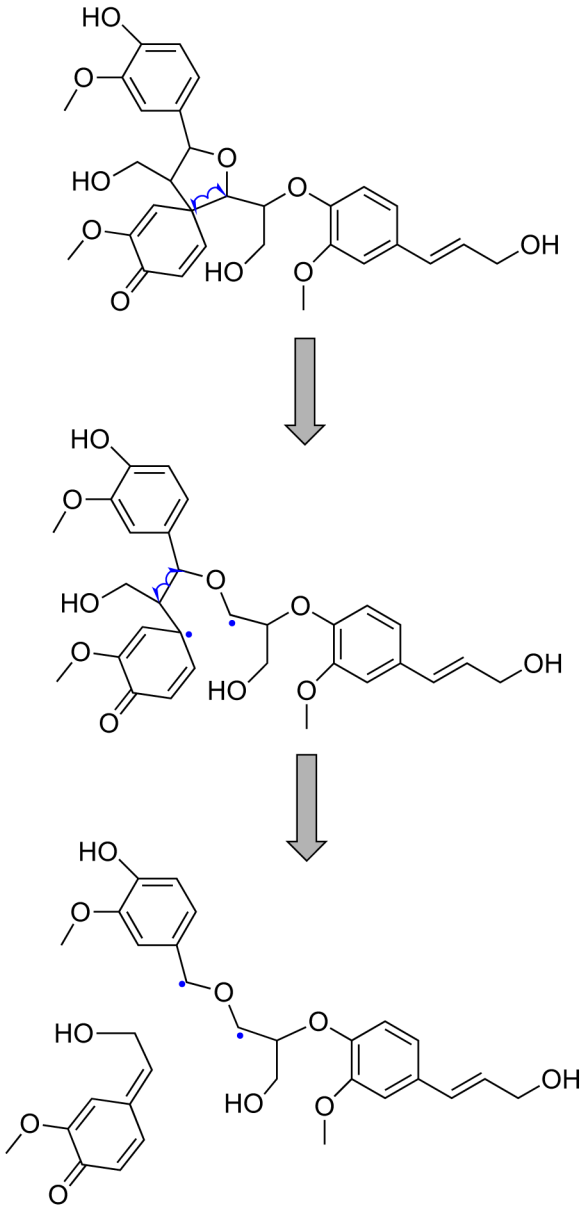

Figure 6. Homolytic bond cleavage pathway **6** with five-membered ring opening of bond C to form a diradical followed by homolytic cleavage of bond A. The diradical rearranges on the ring 1-3-derived products, with ring 2 forming its own closed-shell fragment.

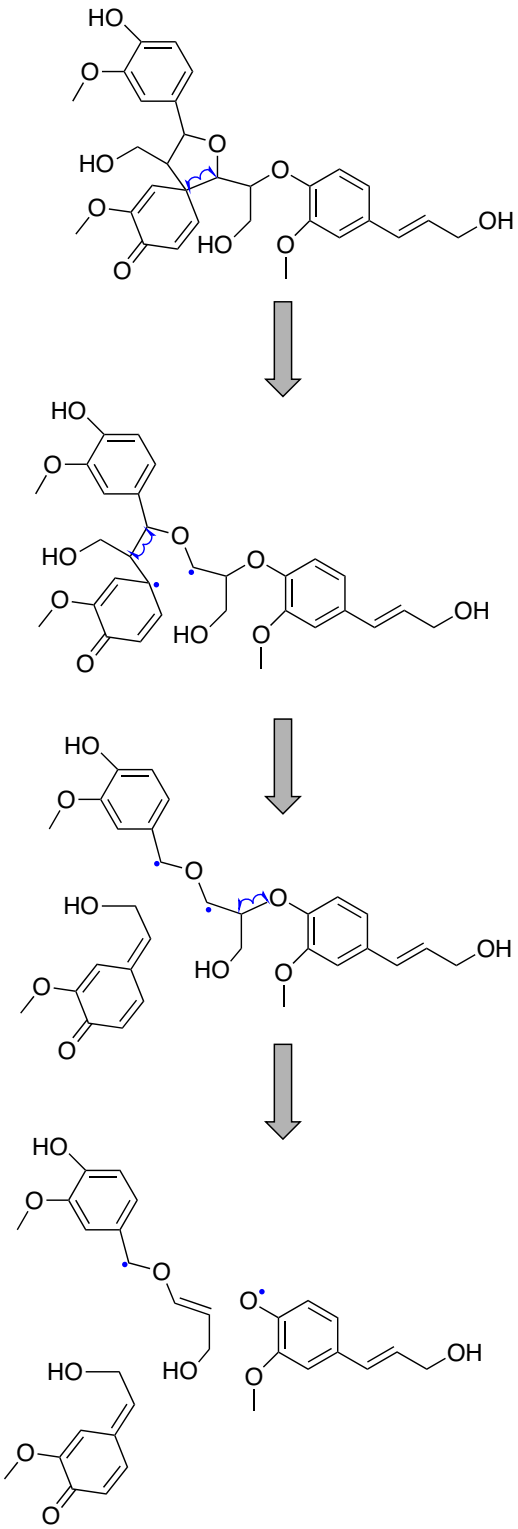

Figure 7. Homolytic bond cleavage pathway **7** with five-membered ring opening of bond C to form a diradical followed by homolytic cleavage of bond A. The diradical rearranges on the ring 1-3-derived products, fragments at bond E, and forms two separated radical fragments. Ring 2 forms its own closed-shell fragment.

The AP dependence is largely derived from the nature of the R2 APs: pulling on R2 AP 2 or AP 3, which are on the far side of R2 from R3 and both oxygen coordinated, leads primarily to cleavage through pathway **7**. For the more proximal R2 APs 1, 4, and 5, cleavage pathway **4** instead predominates, with the closer proximity of these points to bond D possibly explaining the favoring of these APs for C-D cleavage instead of further ring opening. Beyond the R2-dominant pathway statistics, a number of specific R2-R3 AP pairings led primarily to cleavage through pathway **6**, which consists of both C and E cleavage, when the APs were on both the far sides of each ring and on opposing sides/directions of the bond E to maximize the torque felt by that bond (e.g., R2 AP 3 to R3 AP 4 or R2 AP 1 to R3 AP 2 or 3).

Finally, for one AP pair (R2 AP 4 to R2 A3 AP 5) that represents one of the closer sets of attachment points but still in opposing directions, pathway **5** instead predominates (Figure 2). Although we have identified predominant pathways, overall there is significant diversity for each R2-R3 AP pairing that leads to cleavage through any of pathways **4**-**7** (Supporting Information Table S4). In all cases, however, the homolytic ring-opening cleavage of bond C occurs followed by a number of different events that depend upon the AP topology. This observation highlights the benefit of sampling of AP choices as a means to discover depolymerization pathways, as we have previously observed in other lignin motifs[59].

3.c. Energetics of Spirodienone Cleavage Products

We now analyze the differing cleavage pathways by determining the relative energetics of the optimized fragment endpoints with respect to an optimized spirodienone (i.e., the reactant) model. In the case of homolytic bond cleavage, the fragment energies should correspond to that bond's BDE, but in more complex rearrangements, energies of transition states along the

cleavage pathway will become relevant (see Sec 3.d). For each major cleavage pathway, a relatively wide range (up to 1 eV) of optimized fragment energetics is observed (Figure 8). In all cases, the intermediates are grouped according to a qualitative fragmentation pattern, and the closest local minimum is obtained upon geometry optimization of the cleaved fragments. These differences in the relative energy, even for seemingly simple homolytic cleavage (e.g., pathway **2**) span a wide range due to differences in the conformer of the rest of the spirodienone linkage, which would not be captured by standard homolytic bond dissociation energetics studies.

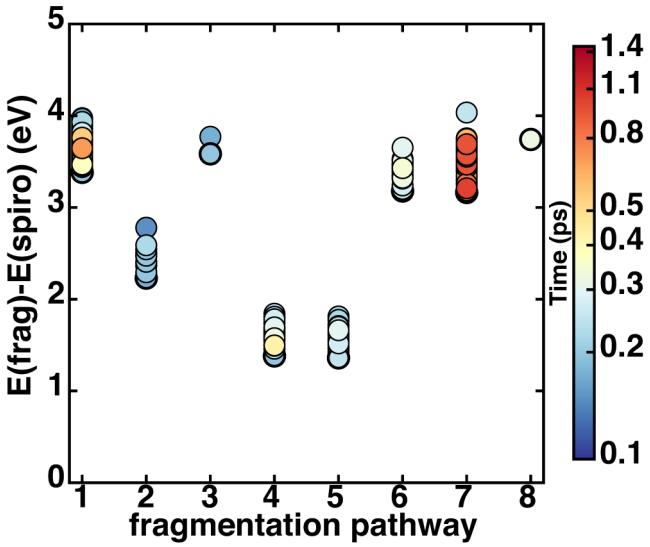

Figure 8. Energy of geometry optimized products (in eV) for the **1**-**8** fragmentation pathways relative to the optimized spirodienone structure. Each cleavage product is colored on a log scale (color bar shown at right) by the time in the simulation at which the cleavage event occurred. The most stable products obtained for each pathway is highlighted with a thicker outline around the circle.

Fragmentation pathways **4** and **5** produce fragments as low as 1 eV higher in energy than the original spirodienone molecule, which makes them also around 1 eV more stable than any other fragmentation pattern. Of the simple homolytic cleavage patterns, the β-O-4-like ether bond in pathway **2** gives products as low as 2 eV compared to the more unfavorable 3-4 eV C-C bond cleavage in pathway **1**. These energetics are consistent with the 2.3-3.1 eV bond

dissociation energies previously computed[35-37, 82] in models of the β-O-4 linkage. Pathway **3** fragments are roughly isoenergetic with pathway **1**, where the two pathways differ by the latter's additional cleavage of a five-membered-ring C-O bond (B) at the same time as cleavage of the C-C bond (D). The final products in the two pathways differ primarily in whether the tetrahydrofuranal five-membered ring opens and stabilizes the radical adjacent to bond B on the alkyl chain or whether the radical remains on the ring, suggesting that ring-opening becomes thermodynamically favorable following C-C bond cleavage.

Pathways **4**-**8** all initiate with homolytic cleavage of the C-C bond in the five-membered spirodienone ring. However, rearrangement in pathways **6**-**8** generally lead to less favorable products (3-4 eV) compared to pathways **4**-**5** (1-2 eV). This difference may be interpreted by examining the major products (see Sec. 3.b) and observing that pathways **4**-**5** introduce aromaticity into the previously non-aromatic six-membered ring of spirodienone, preferring to form diradicals on the previously carbonyl oxygen and the structure backbone. Pathways **6** and **7** preserve the dienone nature of the six membered ring, typically in a nonradical fashion and distribute the radical over the other fragments. Pathway **8** is relatively high in energy, likely due to the formation of four fragments and four radicals, with the highest number of bond cleavages observed in all simulations. We note, however, that the higher number of fragments likely lowers the relative free energy of these products, which was not computed in this study. Thus, the roughly 2 eV stabilization is due to formation of the phenyl ring with aromatic character in pathways **4** and **5**. We will revisit shortly the kinetics of these rearrangements through reaction pathway analysis (see Sec. 3.d).

It is also apparent that slower cleavage events under force do not necessarily correlate to lower energy fragments, as the latest cleavage events (ca. 1-1.4 ps) mostly correspond to the multi-step pathway **7**, which is less thermodynamically favorable than the relatively quick, 100 fs rearrangements apparent for all pathway **5** fragmentation patterns. These timescales should not be interpreted outside of steered MD, as the speed of cleavage events in the presence of a large 4.0 nN force may have little to do with relative rates where mechanical force is not applied. Overall, products of pathways **1**, **3**, **6**, **7**, and **8** all reside about 3-4 eV above the spirodienone ground state, consistent with the 3.9 eV energetic cost of cleaving a C-C bond[83] or, more specifically, β-1 bonds[84] in lignin 2.8-3.0 eV BDEs, whereas the lower energetic cost of pathway **2** is consistent with, but a little lower than, typical ether bond cleavages around 3.2 eV[85].

3.d. Mechanism and Reaction Pathway Analysis

We computed energetic barriers for the eight major dynamically observed cleavage pathways to identify the most kinetically favorable cleavage pathways. In order to identify minimum energy pathways, each bond cleavage event was isolated as an elementary step, and a nudged elastic band calculation was carried out using geometry-optimized fragments obtained from AISMD trajectories (see Sec. 2). Simple homolytic bond cleavage pathway **1** corresponds to a bond D cleavage event with a steep, near-monotonic 3.5 eV barrier that corresponds to nearly the same energetics that would be obtained directly from homolytic BDE estimates (minimum energy pathway shown in Figure 9, intermediate structures in Figure 3, and range of endpoint energetics in Figure 8). The pathway **1** C-C bond cleavage products at the tetrahydrofuran ring (3.2-4.0 eV) were already observed to be less thermodynamically favorable than pathway **2** ether bond cleavage that forms a monolignol radical monomer (2.1-2.8 eV).

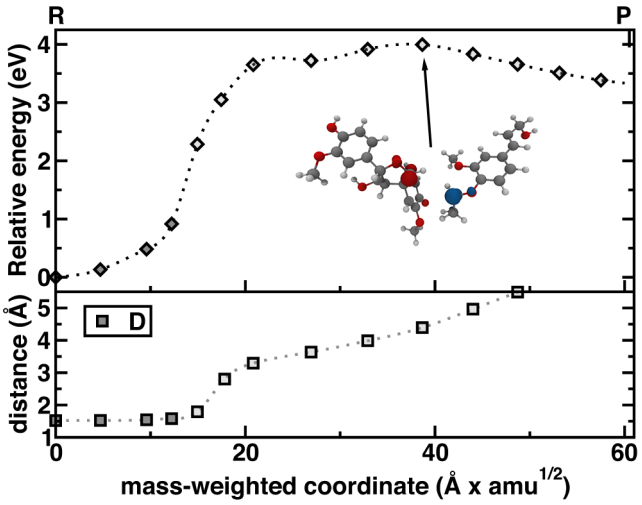

Figure 9. Cleavage pathway **1** reaction coordinate energetics (top) and cleaving bond E distance (bottom). The onset of radical character, as indicated by NBO analysis, is shown as a transition from opaque to translucent symbol fill in both the bond and energy plots. The structure of the highest energy point is annotated and shown inset in ball and stick representation (gray carbon, red oxygen, white hydrogen) with spin density isosurface (iso value = 0.02 e, red for positive spin density and blue for negative spin density).

Analysis of bond E cleavage in pathway **2** (Figure 10) reveals more substantial differences between the reaction barrier (3.0 eV) and products (2.0 eV), suggesting differences in expected kinetics with respect to the direct BDE calculation. The qualitative features of the pathway **2** reaction profile are comparable to what was observed for pathway **1**: radical character is observed at only small displacements from equilibrium (0.1-0.2 Å) bond lengths, corresponding to a steep jump in energy, followed by complete dissociation and preservation of the diradical character (Figures 9 and 10). Analysis of structures along the minimum energy pathway reveals that a fair amount of rotation, which would not be captured in a BDE calculation, mediates the ether bond cleavage, leading at first to a hydrogen bonding interaction formed between the ring 3 oxygen on position 1 with the ring 1 hydroxyl on position 3 (see coordinates provided in the Supporting Information). The final products are instead stabilized by a more favorable ring 1 hydroxyl to ring 3 monolignol oxygen radical hydrogen bond, leading to

lower product energetics. These observations suggest that larger lignin models could likely mediate bond cleavage barriers via earlier formation of stabilizing hydrogen-bonding interactions. Overall, minimum energy pathway analysis confirms expectations that bond E ether cleavage is more kinetically and thermodynamically favorable than bond D C-C cleavage adjacent to the tetrahydrofuran ring.

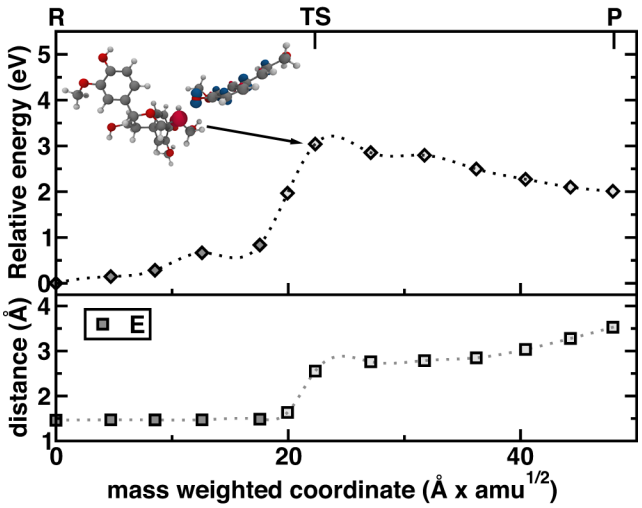

Figure 10. Cleavage pathway **2** reaction coordinate energetics (top) and cleaving bond E distance (bottom). The onset of radical character, as indicated by NBO analysis, is shown as a transition from opaque to translucent symbol fill in both the bond and energy plots. The structure of the highest energy point is annotated and shown inset in ball and stick representation (gray carbon, red oxygen, white hydrogen) with spin density isosurface (iso value = 0.02 e, red for positive spin density and blue for negative spin density).

The rarely observed pathway **3** corresponds to the simultaneous cleavage of D, the C-C bond adjacent to the tetrahydrofuran ring followed by immediate ring-opening through bond B cleavage and migration of the radical adjacent to ring 1 rather than adjacent to ring 3 (Supporting Information Figure S1). During dynamic trajectories, the rapid cleavage events (0.1-0.2 ps, see Figure 8) make it difficult to distinguish the order of bond B and D cleavage. The relative energetics of pathway **3** products with respect to pathway **1** (Figure 8) would suggest that the ring-opening cleavage is barrierless, especially when carried out in concert with the C-C bond

cleavage. However, minimum energy pathway analysis converges to a pathway in which bond B cleavage slightly precedes bond D cleavage, leading to one of the highest observed barriers (5 eV) for any of the eight major pathways, despite the moderate 3 eV product energetics (Figure 11). Follow-up work could focus on on-the-fly control of the dynamics trajectories to both cool and reduce forces on them as soon as a first bond cleavage event is detected in order to observe only downhill rearrangements in order to identify if bond B after D cleavage is in fact barrierless.

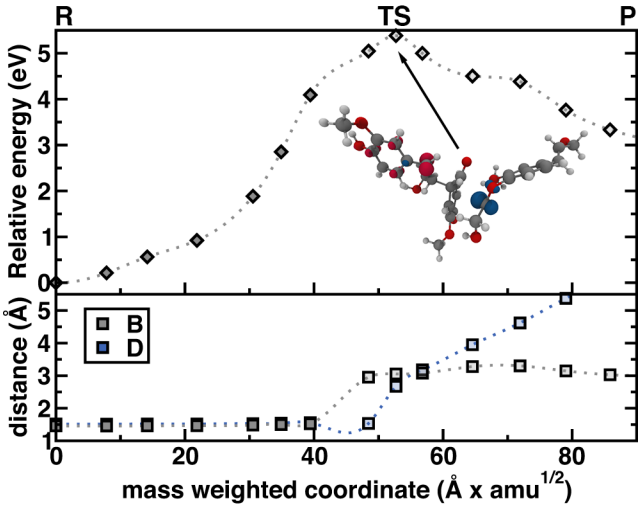

Figure 11. Homolytic bond cleavage pathway **3** minimum energy pathway and characteristic bond cleavage events. The point at which radical character is detected in a bond is indicated by translucent symbols. The structure of the highest energy point is annotated and shown inset in ball and stick representation (gray carbon, red oxygen, white hydrogen) with spin density isosurface (iso value = 0.02 e, red for positive spin density and blue for negative spin density).

Homolytic bond cleavage pathways **4** and **5** represent the most energetically favorable pathways for spirodienone depolymerization. In both cases, optimized products ranged from as low as around 1.1 eV above the intact spirodienone to as high as around 1.9 eV, well below the energy of other fragments. In both cases, bond C cleaves first, opening the tetrhydrofuran ring and leads to the return of aromaticity to the dienone ring 2, driving down the energetics of the products. Pathway **4** may be viewed as particularly beneficial if also kinetically favorable

because it releases a single monolignol radical, providing a path to controlled, high-value products (Figure 4).

Despite originating from optimization of differing dynamical trajectories, barriers for minimum energy pathways **4** and **5** at around 2.5 eV are comparable (Figures 12 and 13). These barriers are lower than the ether bond or other C-C bond cleavages considered thus far. In both cases, the cleavage of the C-C bond in the five-membered ring adjacent to the dienone ring introduces diradical character that favors this cleavage pattern. Namely, there is no radical character on the dienone ring carbon after homolytic C-C cleavage, due to introduction of aromaticity (see TS_1 structures shown in Figures 12 and 13). Instead, that radical has migrated to the oxygen on the newly aromatic six-membered ring, and the remainder of the radical is delocalized over the other carbon atom and adjacent oxygen in the remainder of the in-tact five membered ring. Thus, the introduction of aromaticity into the dienone mediates a lower C-C bond cleavage barrier in addition to stabilizing the intermediate energetics.

Interestingly, in pathway **4**, we observe that the subsequent cleavage of ether bond E becomes nearly barrierless, despite the fact that this cleavage initiates from intermediates that are only around 1.3-1.5 eV above the reactant energies (Figure 12). The low barrier for bond E ether cleavage can also be understood in terms of the migrating radical from carbon-centered in TS_1 to a more stable oxygen-centered radical in TS_2 (Figure 12). Because bond E ether cleavage is coupled to recovery of aromaticity in the dienone ring, it in fact becomes weakly exothermic, with products around 1.1 eV. This energetic profile is quite distinct from what is observed for isolated ether bond E cleavage that previously was observed to be both endothermic by 2 eV and to have a barrier of around 3 eV (Figure 10). The difference here is that bond E ether cleavage in pathway 4 is mediated through a single oxygen radical on bond E, whereas two radicals must

form on either side of cleaved bond E in pathway **2** (see structures in Figure 10). Thus, observations in pathway **4** highlight that BDEs alone are insufficient for identifying lignin depolymerization pathways when intermediate rearrangement occurs.

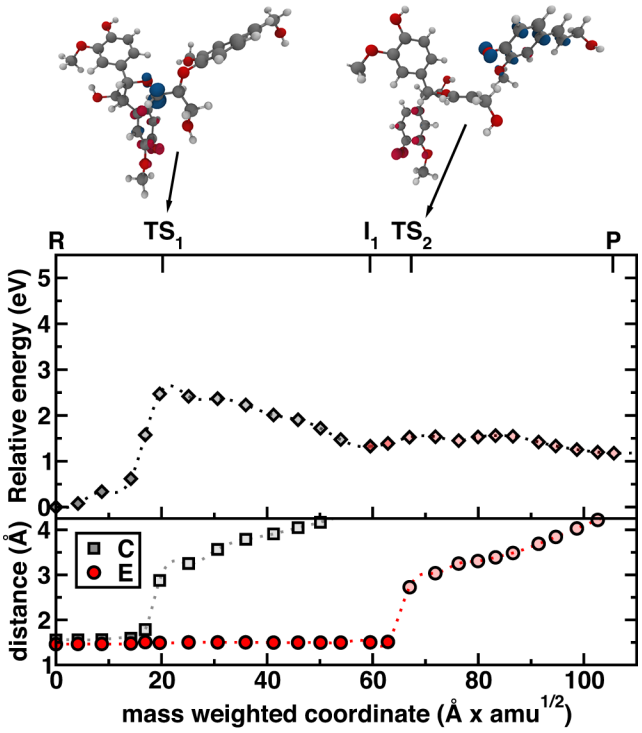

Figure 12. Cleavage pathway **4** reaction coordinate energetics in two steps – bond C cleavage (gray diamonds) and subsequent bond E cleavage (red diamonds) (top) and cleaving C (gray squares) and E (red circles) bond distances (bottom). The onset of radical character, as indicated by NBO analysis, is shown as a transition from opaque to translucent symbol fill in both the bond and energy plots. The structure of the highest energy points for each step are annotated and shown above in ball and stick representation (gray carbon, red oxygen, white hydrogen) with spin density isosurface (iso value = 0.02 e, red for positive spin density and blue for negative spin density).

Conversely, pathway **5** energetics for the subsequent cleavage of the ether bond B in the tetrahydrofuran ring (Figure 5) are not as kinetically favorable as for bond E cleavage in pathway **4** (Figure 13). The high barrier for this step can be understood in terms of the energetic cost of rearrangement required upon bond cleavage that again would also not be captured by a BDE calculation. Namely, the sp^3 carbon on bond B that bridges rings 1 and 2 has a hydrogen atom

that must rearrange to form an sp^2 radical when the bond B cleaves. The initially poor placement of this atom is what corresponds to the increased barrier height for the bond B cleavage (see pathway structures in Figure 13 and the Supporting Information). Analysis of the spin densities also reveals that the carbon-centered radical formed during bond B cleavage is unfavorable compared to ether bond cleavages in which the radical may be stabilized on an oxygen atom (pathway **4**). Indeed, pathway **3** consists of simultaneous bond B and D cleavage and has even higher barrier heights for this simultaneous cleavage due to the lack of stabilization by an oxygen-centered radical (Figure 11). Overall, final products are indeed stable for both pathways **4** and **5**, as observed from both isolated geometry optimizations (Figure 8) and the minimum energy pathway analysis (Figures 12 and 13).

Despite the somewhat favorable energetics of pathway **4** and **5** products (1 eV above the reactant ground state), none of the pathways have depolymerization products that are more stable than the reactants. High reverse reaction barriers suggest that the products will not revert to reactants, but it is likely that such products from these pathways would continue to react. In order to preserve such products, hydrogen atom sources, e.g. from water or additional lignin would be expected to react with the formed radicals to form stable and value-added products such as the monolignol produced in pathway **4**. The relative stability of unreactive products could be sensitive to inhibitor choice. If molecular oxygen were instead used to stabilize radicals, one might expect differing stabilization of carbon-centered radicals versus the oxygen-centered radical in pathways **4**, **5**, and **7**.

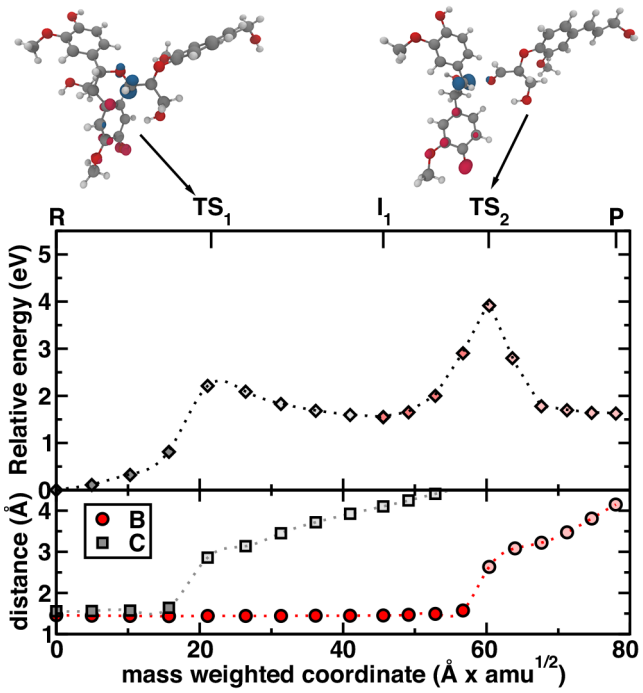

Figure 13. Cleavage pathway **5** reaction coordinate energetics in two steps – bond C cleavage (gray diamonds) and subsequent bond B cleavage (red diamonds) (top) and cleaving C (gray squares) and B (red circles) bond distances (bottom). The onset of radical character, as indicated by NBO analysis, is shown as a transition from opaque to translucent symbol fill in both the bond and energy plots. The structure of the highest energy points for each step are annotated and shown above in ball and stick representation (gray carbon, red oxygen, white hydrogen) with spin density isosurface (iso value = 0.02 e, red for positive spin density and blue for negative spin density).

In only one case, pathway **8**, we observed a cleavage pathway that combined initial bond C cleavage with subsequent concerted cleavage of both bonds B and E (intermediate structures shown in Supporting Information Figure S2). This fragmentation pattern produces the monolignol radical as well as a small fragment radical, producing four overall carbon radicals on three fragments compared to the other pathways that are only observed to form either two radical fragments or one diradical fragment and one closed shell fragment. Reaction pathway analysis reveals comparable bond C cleavage energetics with a barrier around 2 eV and products around 1.5 eV (Supporting Information Figure S3). The bond B and E cleavage occur rapidly, but bond E is broken slightly before bond B, making the initial part of the second reaction step

straightforward to compare to pathway **4** (Figure 12). Indeed, analysis up to the point where E has cleaved but not B reveal comparable energetics between pathways **4** and **8**, but bond B cleavage is destabilizing with a barrier around 3.8 eV overall or about 2.3 eV for the single step and is quite endothermic (Supporting Information Figure S3). Nevertheless, bond B cleavage following E cleavage is slightly more favorable than direct C and B cleavage observed in pathway **5** (Figure 13). Thus, comparison of the three pathways suggests that ring opening to introduce aromaticity into the dienone ring (C cleavage) followed by ether bond cleavage E is the most kinetically favorable reaction pathway, but under some reaction conditions further bond cleavage may be relatively favorable.

In cleavage pathway **6**, C-C bond cleavage (bond C) to form ring-opened products is followed by a second C-C bond cleavage in the original tetrahydrofuran ring (Figure 6). This double bond cleavage leads to a closed shell dienone ring monomer being released, unlike the previous pathways. Analysis of the minimum energy pathway reaction energetics reveals that the second C-C bond cleavage (bond A) has a comparable 2 eV barrier to the first bond cleavage (Figure 14). It might be expected that the initial bond cleavage has a lower barrier as it relieves ring strain, whereas the second cleavage does not. Overall, formation of the dienone fragment in pathway **6** without introduction of aromaticity, as in pathways **4** and **5**, is both less thermodynamically and kinetically favorable, as observed through geometry optimizations (Figure 8) and reaction pathway analysis (Figure 14).

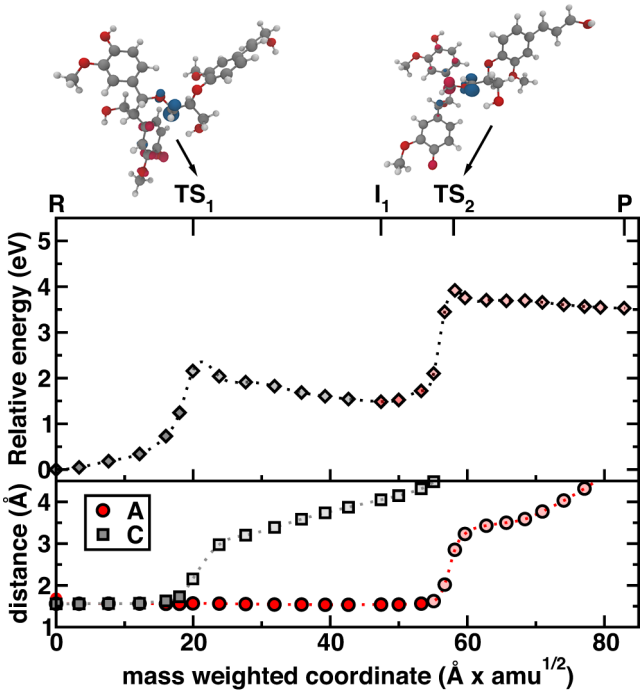

Figure 14. Cleavage pathway **6** reaction coordinate energetics in two steps – bond C cleavage (gray diamonds) and subsequent bond A cleavage (red diamonds) (top) and cleaving C (gray squares) and A (red circles) bond distances (bottom). The onset of radical character, as indicated by NBO analysis, is shown as a transition from opaque to translucent symbol fill in both the bond and energy plots. The structure of the highest energy points for each step are annotated and shown above in ball and stick representation (gray carbon, red oxygen, white hydrogen) with spin density isosurface (iso value = 0.02 e, red for positive spin density and blue for negative spin density).

A second class of bond C-followed-by-A cleavage events was observed in pathway **7** (Figure 7), which is at first identical to pathway **6** (Figure 6) but then leads to subsequent ether bond E cleavage present in pathways **2** and **4** (Figures 3 and 4). We previously identified that in pathway 4 the bond E ether cleavage became barrierless when coupled to restored aromaticity of the dienone ring. However, in pathway **7**, the dienone ring does not become aromatic, suggesting that the bond E cleavage may be less favorable. The first two uncoupled steps of pathway **7** are energetically and structurally identical to pathway **6**, leading to a 2.5 eV barrier for bond C cleavage, followed by a second 2 eV barrier (4 eV overall) for bond A cleavage (Figure 15). The

subsequent cleavage of the ether bond E is not strictly barrierless at about 0.5-1.0 eV, but it is considerably lower than ether bond cleavage in isolation (3 eV in pathway **2** in Figure 10). The lower barrier here likely comes from the restoration of a double bond rather than radical character in ring 1 and tetrahydrofuran C-C bond (Figure 7) adjacent to the newly formed monolignol radical. The overall barriers for this pathway are indeed lower than would be estimated based on BDEs alone for each of the four cleaved bonds.

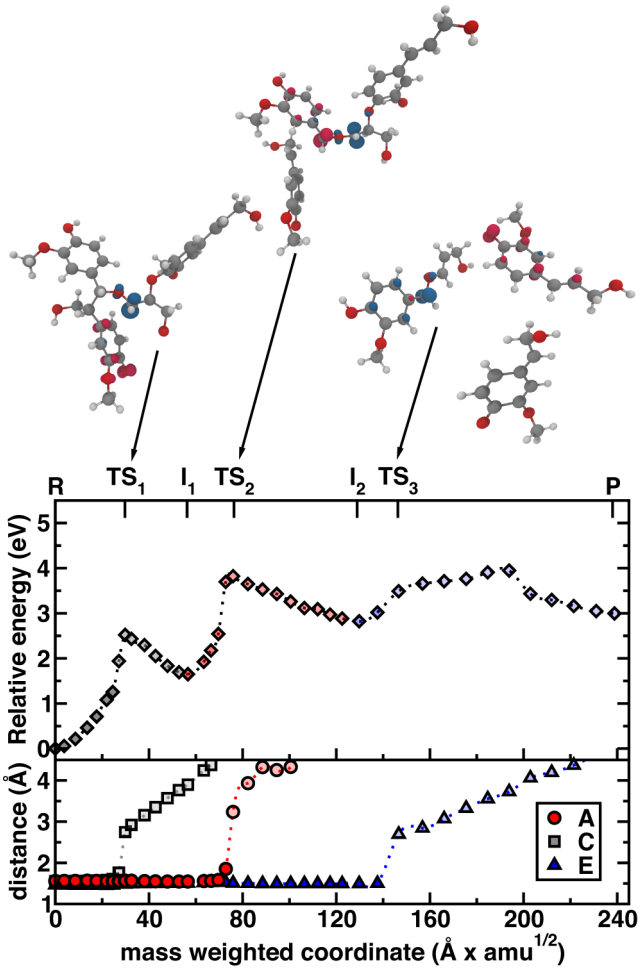

Figure 15. Cleavage pathway **7** reaction coordinate energetics in three steps – bond C cleavage (gray diamonds) followed by subsequent bond A cleavage (red diamonds) and bond E cleavage (blue diamonds) (top) and cleaving C (gray squares), A (red circles), and E (blue triangles) bond distances (bottom). The onset of radical character, as indicated by NBO analysis, is shown as a transition from opaque to translucent symbol fill in both the bond and energy plots. The structure of the highest energy points for each step are annotated and shown above in ball and stick

representation (gray carbon, red oxygen, white hydrogen) with spin density isosurface (iso value = 0.02 e, red for positive spin density and blue for negative spin density).

Overall, comparison of eight unique cleavage pathways of the spirodienone linkage has revealed that order of bond cleavage alters the kinetics and thermodynamics of the rearranging intermediates. In particular, introduction of aromaticity into the dienone ring in pathways **4** and **5** produces products only 1 eV above the ground state spirodienone structure and well below the energetic cost that would be predicted by standard BDE estimation that does not consider radical or bond rearrangement. Comparison of minimum energy pathways obtained from the dynamics trajectories across the pathways **1**-**8** is internally consistent, suggesting that bond E ether cleavage may be near barrierless if it occurs after bond C cleavage, as in pathways **4** and **7**. Thus, catalyst design targeting tetrahydrofuran ring opening at the C-C bond could be a fruitful way to cleave lignin branches, recovering simpler oligomers for further processing.

4. Conclusions

We have presented an *ab initio* steered molecular dynamics (AISMD) study of the potential depolymerization pathways of the recently discovered spirodienone lignin linkage. In addition to high heterogeneity, branching in unprocessed lignin is one of the key aspects of the biopolymer that make it difficult to depolymerize into a narrow distribution of products. The AISMD approach has been demonstrated to be a fruitful one to discover a number of unique pathways for depolymerization that could be further made more favorable through targeted catalyst design. Namely, of the 750 dynamics pathways carried out with varied pulling points, eight unique pathways were observed through combinations of cleavage of five bonds in spirodienone.

Analysis of the types of chosen attachment points in the steered MD analysis demonstrated that ring 2 to ring 3 AP combinations were more fruitful for generating complex lignin depolymerization pathways, as opposed to the simple, single step homolytic dissociation pathways **1** and **2** that predominated through ring 1 to ring 3 AP combinations or ring 1 to ring 2 AP pairs that yielded no cleavage. This analysis may be translated in chemical terms to reveal that the ether-adjacent side of the tetrahydrofuran ring in the spirodienone linkage is more amenable to uncatalyzed or catalyzed depolymerization.

Energetic analysis of the products of these dynamic cleavage pathways revealed that products in pathways **4** and **5** were only somewhat higher in energy than the intact spirodienone linkage at around 1 eV. These products are considerably lower in energy than the other 6 pathways that were around 2-4 eV above the spirodienone energy, consistent with standard expectations for the energetic cost of single C-C or C-O bond cleavage from bond dissociation energies. Analysis of the electronic structure of these products revealed rearrangement of the non-aromatic dienone ring to recover aromaticity.

Minimum energy pathway analysis suggested that BDE analysis alone may be insufficient in some cases (e.g., pathway **2**) where products of transition states may rearrange to form stabilizing hydrogen bonds, especially in larger models of lignin than were studied in this work. Most importantly, we identified kinetically and thermodynamically favorable bond E ether cleavage to follow barrierlessly upon bond C tetrahydrofuran ring opening (pathway **4**) in a manner that is likely to be made even more favorable with rational catalyst design. Generally, reintroduction of closed shell character was favored in pathway **7** as well, where bond E cleavage was favored following bond C and A cleavage as it enabled formation of a C-C double bond. This analysis reveals that the order of bond cleavage events and the dynamic rearrangement that

occurs is a critical component of building mechanistic understanding of how complex lignin linkages depolymerize.

The mechanochemical deformation at high forces can give rise to relatively high energy pathways that may be unfavorable (bond B cleavage in **5**) alongside more favorable pathways (bond E cleavage in **4**). Analysis of the frequency of different pathways does indicate however that pathway **4** is relatively commonly sampled in our AISMD simulations. A route to quantitative correspondence between probabilities in ring pulling statistics and the most energetically favorable pathways would be in the use of lower forces and longer trajectories. Overall, this sampling approach shows great promise for discovering depolymerization pathways in complex polymers.

ASSOCIATED CONTENT

Supporting Information. Single point energies obtained with alternate exchange-correlation functional choice; statistics on trajectories for cleavage scheme by AP; ring 1-3 cleavage data by AP and ring 2-3 cleavage data by AP; energy of optimized fragments sorted by cleavage scheme; schematic of homolytic bond cleavage pathways 3 and 8; minimum energy pathways and bond distances for pathway 8; structures along all cleavage minimum energy pathways 1-8. This material is available free of charge via the Internet at http://pubs.acs.org.

AUTHOR INFORMATION

Corresponding Author

*email: hjkulik@mit.edu phone: 617-253-4584

Notes

The authors declare no competing financial interest.

ACKNOWLEDGMENT

This work was supported by an MIT Research Support Corporation Reed Grant. Partial support is also acknowledged from the National Science Foundation under grant number ECCS-1449291. H.J.K. holds a Career Award at the Scientific Interface from the Burroughs Wellcome Fund. This work was carried out in part using computational resources from the Extreme Science and Engineering Discovery Environment (XSEDE), which is supported by National Science Foundation grant number ACI-1053575. The authors thank Adam H. Steeves for providing a critical reading of the manuscript.

References

1. Klass, D. L., Biomass for Renewable Energy and Fuels. *Encycl. Energy* **2004,** *1*, 193-212.
2. Gayubo, A. G.; Valle, B.; Aguayo, A. T.; Olazar, M.; Bilbao, J., Pyrolytic Lignin Removal for the Valorization of Biomass Pyrolysis Crude Bio-Oil by Catalytic Transformation. *J. Chem. Technol. Biotechnol.* **2010,** *85*, 132-144.
3. Bruijnincx, P. C. A.; Weckhuysen, B. M., Biomass Conversion: Lignin up for Break-Down. *Nat. Chem.* **2014,** *6*, 1035-1036.
4. Linger, J. G.; Vardon, D. R.; Guarnieri, M. T.; Karp, E. M.; Hunsinger, G. B.; Franden, M. A.; Johnson, C. W.; Chupka, G.; Strathmann, T. J.; Pienkos, P. T., et al., Lignin Valorization through Integrated Biological Funneling and Chemical Catalysis. *Proc. Natl. Acad. Sci. U. S. A.* **2014,** *111*, 12013-12018.
5. Ragauskas, A. J.; Beckham, G. T.; Biddy, M. J.; Chandra, R.; Chen, F.; Davis, M. F.; Davison, B. H.; Dixon, R. A.; Gilna, P.; Keller, M., et al., Lignin Valorization: Improving Lignin Processing in the Biorefinery. *Science* **2014,** *344*, 6185.
6. Strassberger, Z.; Tanase, S.; Rothenberg, G., The Pros and Cons of Lignin Valorisation in an Integrated Biorefinery. *RSC Adv.* **2014,** *4*, 25310-25318.
7. Turkenburg, W. C.; Beurskens, J.; Faaij, A.; Fraenkel, P.; Fridleifsson, I.; Lysen, E.; Mills, D.; Moreira, J. R.; Nilsson, L. J.; Schaap, A., Renewable Energy Technologies. *World energy assessment: Energy and the challenge of sustainability* **2000**, 219-272.
8. Dutta, S.; Wu, K. C. W.; Saha, B., Emerging Strategies for Breaking the 3D Amorphous Network of Lignin. *Catal. Sci. Technol.* **2014,** *4*, 3785-3799.
9. Huber, G. W.; Iborra, S.; Corma, A., Synthesis of Transportation Fuels from Biomas: Chemistry, Catalysts, and Engineering. *Chem. Rev.* **2006,** *106*, 4044-4098.

10. Kersten, S.; Garcia-Perez, M., Recent Developments in Fast Pyrolysis of Ligno-Cellulosic Materials. *Curr. Opin. Biotechnol.* **2013,** *24*, 414-420.
11. Zhou, X.; Nolte, M. W.; Shanks, B. H.; Broadbelt, L. J., Experimental and Mechanistic Modeling of Fast Pyrolysis of Neat Glucose-Based Carbohydrates. 2. Validation and Evaluation of the Mechanistic Model. *Ind. Eng. Chem. Res.* **2014,** *53*, 13290-13301.
12. Azadi, P.; Carrasquillo-Flores, R.; Pagan-Torres, Y. J.; Gurbuz, E. I.; Farnood, R.; Dumesic, J. A., Catalytic Conversion of Biomass Using Solvents Derived from Lignin. *Green Chem.* **2012,** *14*, 1573-1576.
13. Johnson, C. W.; Beckham, G. T., Aromatic Catabolic Pathway Selection for Optimal Production of Pyruvate and Lactate from Lignin. *Metab. Eng.* **2015,** *28*, 240-247.
14. Zaheer, M.; Kempe, R., Catalytic Hydrogenolysis of Aryl Ethers: A Key Step in Lignin Valorization to Valuable Chemicals. *ACS Catal.* **2015,** *5*, 1675-1684.
15. Prasomsri, T.; Shetty, M.; Murugappan, K.; Román-Leshkov, Y., Insights into the Catalytic Activity and Surface Modification of MoO 3 During the Hydrodeoxygenation of Lignin-Derived Model Compounds into Aromatic Hydrocarbons under Low Hydrogen Pressures. *Energy Environ. Sci.* **2014,** *7*, 2660-2669.
16. Gilormini, P.; Richaud, E.; Verdu, J., A Statistical Theory of Polymer Network Degradation. *Polymer* **2014,** *55*, 3811-3817.
17. Zakzeski, J.; Jongerius, A. L.; Bruijnincx, P. C. A.; Weckhuysen, B. M., Catalytic Lignin Valorization Process for the Production of Aromatic Chemicals and Hydrogen. *ChemSusChem* **2012,** *5*, 1602-1609.
18. Roberts, V. M.; Stein, V.; Reiner, T.; Lemonidou, A.; Li, X.; Lercher, J. A., Towards Quantitative Catalytic Lignin Depolymerization. *Chem. Eur. J.* **2011,** *17*, 5939-5948.
19. Xia, G.-G.; Chen, B.; Zhang, R.; Zhang, Z. C., Catalytic Hydrolytic Cleavage and Oxy-Cleavage of Lignin Linkages. *J. Mol. Catal. A: Chem.* **2014,** *388–389*, 35-40.
20. Sturgeon, M. R.; Kim, S.; Lawrence, K.; Paton, R. S.; Chmely, S. C.; Nimlos, M.; Foust, T. D.; Beckham, G. T., A Mechanistic Investigation of Acid-Catalyzed Cleavage of Aryl-Ether Linkages: Implications for Lignin Depolymerization in Acidic Environments. *ACS Sustainable Chem. Eng.* **2014,** *2*, 472-485.
21. Rahimi, A.; Ulbrich, A.; Coon, J. J.; Stahl, S. S., Formic-Acid-Induced Depolymerization of Oxidized Lignin to Aromatics. *Nature* **2014,** *515*, 249-252.
22. Wen, J.-L.; Yuan, T.-Q.; Sun, S.-L.; Xu, F.; Sun, R.-C., Understanding the Chemical Transformations of Lignin During Ionic Liquid Pretreatment. *Green Chem.* **2014,** *16*, 181-190.
23. Feghali, E.; Cantat, T., Unprecedented Organocatalytic Reduction of Lignin Model Compounds to Phenols and Primary Alcohols Using Hydrosilanes. *Chem. Commun. (Cambridge, U. K.)* **2014,** *50*, 862-865.
24. Nguyen, J. D.; Matsuura, B. S.; Stephenson, C. R. J., A Photochemical Strategy for Lignin Degradation at Room Temperature. *J. Am. Chem. Soc.* **2014,** *136*, 1218-1221.
25. Fujimoto, A.; Matsumoto, Y.; Chang, H.-M.; Meshitsuka, G., Quantitative Evaluation of Milling Effects on Lignin Structure During the Isolation Process of Milled Wood Lignin. *J. Wood Sci.* **2005,** *51*, 89-91.
26. Hanson, S. K.; Baker, R. T.; Gordon, J. C.; Scott, B. L.; Thorn, D. L., Aerobic Oxidation of Lignin Models Using a Base Metal Vanadium Catalyst. *Inorg. Chem.* **2010,** *49*, 5611-5618.
27. Hicks, J. C., Advances in C-O Bond Transformations in Lignin-Derived Compounds for Biofuels Production. *J. Phys. Chem. Lett.* **2011,** *2*, 2280-2287.

28. Nichols, J. M.; Bishop, L. M.; Bergman, R. G.; Ellman, J. A., Catalytic C-O Bond Cleavage of 2-Aryloxy-1-Arylethanols and Its Application to the Depolymerization of Lignin-Related Polymers. *J. Am. Chem. Soc.* **2010,** *132*, 12554-12555.
29. Sergeev, A. G.; Hartwig, J. F., Selective, Nickel-Catalyzed Hydrogenolysis of Aryl Ethers. *Science* **2011,** *332*, 439-443.
30. Son, S.; Toste, F. D., Non-Oxidative Vanadium-Catalyzed C-O Bond Cleavage: Application to Degradation of Lignin Model Compounds. *Angew. Chem., Int. Ed.* **2010,** *49*, 3791-3794.
31. Bugg, T. D. H.; Ahmad, M.; Hardiman, E. M.; Singh, R., The Emerging Role for Bacteria in Lignin Degradation and Bio-Product Formation. *Curr. Opin. Biotechnol.* **2011,** *22*, 394-400.
32. Pandey, M. P.; Kim, C. S., Lignin Depolymerization and Conversion: A Review of Thermochemical Methods. *Chem. Eng. Technol.* **2011,** *34*, 29-41.
33. Song, Q.; Wang, F.; Cai, J.; Wang, Y.; Zhang, J.; Yu, W.; Xu, J., Lignin Depolymerization (LDP) in Alcohol over Nickel-Based Catalysts via a Fragmentation–Hydrogenolysis Process. *Energy Environ. Sci.* **2013,** *6*, 994-1007.
34. Parsell, T.; Yohe, S.; Degenstein, J.; Jarrell, T.; Klein, I.; Gencer, E.; Hewetson, B.; Hurt, M.; Kim, J. I.; Choudhari, H., et al., A Synergistic Biorefinery Based on Catalytic Conversion of Lignin Prior to Cellulose Starting from Lignocellulosic Biomass. *Green Chem.* **2015,** *17*, 1492-1499.
35. Kim, S.; Chmely, S. C.; Nimos, M. R.; Bomble, Y. J.; Foust, T. D.; Paton, R. S.; Beckham, G. T., Computational Study of Bond Dissociation Enthalpies for a Large Range of Native and Modified Lignins. *J. Phys. Chem. Lett.* **2011,** *2*, 2846-2852.
36. Parthasarathi, R.; Romero, R. A.; Redondo, A.; Gnanakaran, S., Theoretical Study of the Remarkably Diverse Linkages in Lignin. *J. Phys. Chem. Lett.* **2011,** *2*, 2660-2666.
37. Younker, J. M.; Beste, A.; Buchanan, A. C., III, Computational Study of Bond Dissociation Enthalpies for Substituted Ss-O-4 Lignin Model Compounds. *ChemPhysChem* **2011,** *12*, 3556-3565.
38. Beste, A.; Buchanan, A. C., III; Harrison, R. J., Computational Prediction of Alpha/Beta Selectivities in the Pyrolysis of Oxygen-Substituted Phenethyl Phenyl Ethers. *J. Phys. Chem. A* **2008,** *112*, 4982-4988.
39. Beste, A.; Buchanan, A. C., III, Computational Study of Bond Dissociation Enthalpies for Lignin Model Compounds. Substituent Effects in Phenethyl Phenyl Ethers. *J. Org. Chem.* **2009,** *74*, 2837-2841.
40. Elder, T., Quantum Chemical Determination of Young's Modulus of Lignin. Calculations on a Beta-O-4' Model Compound. *Biomacromolecules* **2007,** *8*, 3619-3627.
41. Chen, W.; Lickfield, G. C.; Yang, C. Q., Molecular Modeling of Cellulose in Amorphous State. Part I: Model Building and Plastic Deformation Study. *Polymer* **2004,** *45*, 1063-1071.
42. Eichhorn, S. J.; Young, R. J.; Davies, G. R., Modeling Crystal and Molecular Deformation in Regenerated Cellulose Fibers. *Biomacromolecules* **2005,** *6*, 507-513.
43. Kroonbatenburg, L. M. J.; Kroon, J.; Northolt, M. G., Chain Modulus and Intramolecular Hydrogen-Bonding in Native and Regenerated Cellulose Fibers. *Polym. Commun.* **1986,** *27*, 290-292.
44. Simon, J. P.; Eriksson, K. E. L., The Significance of Intra-Molecular Hydrogen Bonding in the Beta-O-4 Linkage of Lignin. *J. Mol. Struct.* **1996,** *384*, 1-7.

45. Beste, A.; Buchanan, A. C., III, Kinetic Analysis of the Phenyl-Shift Reaction in Beta-O-4 Lignin Model Compounds: A Computational Study. *J. Org. Chem.* **2011,** *76*, 2195-2203.
46. Beste, A.; Buchanan, A. C., III, Role of Carbon-Carbon Phenyl Migration in the Pyrolysis Mechanism of Beta-O-4 Lignin Model Compounds: Phenethyl Phenyl Ether and Alpha-Hydroxy Phenethyl Phenyl Ether. *J. Phys. Chem. A* **2012,** *116*, 12242-12248.
47. Beste, A.; Buchanan, A. C., III, Kinetic Simulation of the Thermal Degradation of Phenethyl Phenyl Ether, a Model Compound for the Beta-O-4 Linkage in Lignin. *Chem. Phys. Lett.* **2012,** *550*, 19-24.
48. Beste, A.; Buchanan, A. C., III, Computational Investigation of the Pyrolysis Product Selectivity for Alpha-Hydroxy Phenethyl Phenyl Ether and Phenethyl Phenyl Ether: Analysis of Substituent Effects and Reactant Conformer Selection. *J. Phys. Chem. A* **2013,** *117*, 3235-3242.
49. Beste, A., ReaxFF Study of the Oxidation of Lignin Model Compounds for the Most Common Linkages in Softwood in View of Carbon Fiber Production. *J. Phys. Chem. A* **2014,** *118*, 803-814.
50. Hough, B. R.; Schwartz, D. T.; Pfaendtner, J., Detailed Kinetic Modeling of Lignin Pyrolysis for Process Optimization. *Ind. Eng. Chem. Res.* **2016,** *55*, 9147-9153.
51. Deuss, P. J.; Barta, K., From Models to Lignin: Transition Metal Catalysis for Selective Bond Cleavage Reactions. *Coord. Chem. Rev.* **2016,** *306*, 510-532.
52. Liu, C.; Peterson, C.; Wilson, A. K., C–O Bond Cleavage of Dimethyl Ether by Transition Metal Ions: A Systematic Study on Catalytic Properties of Metals and Performance of DFT Functionals. *J. Phys. Chem. A* **2013,** *117*, 5140-5148.
53. Liu, C.; Wilson, A. K., Cleavage of the β O 4 Linkage of Lignin Using Group 8 Pincer Complexes: A DFT Study. *J. Mol. Catal. A: Chem.* **2015,** *399*, 33-41.
54. Oyedepo, G. A.; Wilson, A. K., Oxidative Addition of the Cα- Cβ Bond in β-O-4 Linkage of Lignin to Transition Metals Using a Relativistic Pseudopotential-Based Ccca-Oniom Method. *ChemPhysChem* **2011,** *12*, 3320-3330.
55. Wang, J.; Liu, L.; Wilson, A. K., Oxidative Cleavage of the β-O-4 Linkage of Lignin by Transition Metals: Catalytic Properties and the Performance of Density Functionals. *J. Phys. Chem. A* **2016,** *120*, 737-746.
56. Janesko, B. G., Acid-Catalyzed Hydrolysis of Lignin Beta-O-4 Linkages in Ionic Liquid Solvents: A Computational Mechanistic Study. *Phys. Chem. Chem. Phys.* **2014,** *16*, 5423-5433.
57. Janesko, B. G., Modeling Interactions between Lignocellulose and Ionic Liquids Using DFT-D. *Phys. Chem. Chem. Phys.* **2011,** *13*, 11393-11401.
58. Gardrat, C.; Ruggiero, R.; Rayez, M.-T.; Rayez, J.-C.; Castellan, A., Experimental and Theoretical Studies of the Thermal Degradation of a Phenolic Dibenzodioxocin Lignin Model. *Wood Sci. Technol.* **2013,** *47*, 27-41.
59. Mar, B. D.; Qi, H. W.; Liu, F.; Kulik, H. J., Ab Initio Screening Approach for the Discovery of Lignin Polymer Breaking Pathways. *J. Phys. Chem. A* **2015,** *119*, 6551-6562.
60. Rinaldi, R.; Jastrzebski, R.; Clough, M. T.; Ralph, J.; Kennema, M.; Bruijnincx, P. C.; Weckhuysen, B. M., Paving the Way for Lignin Valorisation: Recent Advances in Bioengineering, Biorefining and Catalysis. *Angew. Chem., Int. Ed.* **2016,** *55*, 1521-3773.
61. Davis, D. A.; Hamilton, A.; Yang, J.; Cremar, L. D.; Van Gough, D.; Potisek, S. L.; Ong, M. T.; Braun, P. V.; Martinez, T. J.; White, S. R., et al., Force-Induced Activation of Covalent Bonds in Mechanoresponsive Polymeric Materials. *Nature* **2009,** *459*, 68-72.

62. Ong, M. T.; Leiding, J.; Tao, H.; Virshup, A. M.; Martinez, T. J., First Principles Dynamics and Minimum Energy Pathways for Mechanochemical Ring Opening of Cyclobutene. *J. Am. Chem. Soc.* **2009,** *131*, 6377-6379.
63. Kryger, M. J.; Ong, M. T.; Odom, S. A.; Sottos, N. R.; White, S. R.; Martinez, T. J.; Moore, J. S., Masked Cyanoacrylates Unveiled by Mechanical Force. *J. Am. Chem. Soc.* **2010,** *132*, 4558-4559.
64. Lenhardt, J. M.; Ong, M. T.; Choe, R.; Evenhuis, C. R.; Martinez, T. J.; Craig, S. L., Trapping a Diradical Transition State by Mechanochemical Polymer Extension. *Science* **2010,** *329*, 1057-1060.
65. Lenhardt, J. M.; Ogle, J. W.; Ong, M. T.; Choe, R.; Martinez, T. J.; Craig, S. L., Reactive Cross-Talk between Adjacent Tension-Trapped Transition States. *J. Am. Chem. Soc.* **2011,** *133*, 3222-3225.
66. Diesendruck, C. E.; Peterson, G. I.; Kulik, H. J.; Kaitz, J. A.; Mar, B. D.; May, P. A.; White, S. R.; Martínez, T. J.; Boydston, A. J.; Moore, J. S., Mechanically Triggered Heterolytic Unzipping of a Low-Ceiling-Temperature Polymer. *Nat. Chem.* **2014,** *6*, 623-628.
67. Wang, J.; Kouznetsova, T. B.; Kean, Z. S.; Fan, L.; Mar, B. D.; Martínez, T. J.; Craig, S. L., A Remote Stereochemical Lever Arm Effect in Polymer Mechanochemistry. *J. Am. Chem. Soc.* **2014,** *136*, 15162-15165.
68. Zhang, L.; Gellerstedt, G., NMR Observation of a New Lignin Structure, a Spiro-Dienone. *Chem. Commun. (Cambridge, U. K.)* **2001**, 2744-2745.
69. Zhang, L.; Gellerstedt, G.; Ralph, J.; Lu, F., NMR Studies on the Occurrence of Spirodienone Structures in Lignins. *J. Wood Chem. Technol.* **2006,** *26*, 65-79.
70. Sette, M.; Wechselberger, R.; Crestini, C., Elucidation of Lignin Structure by Quantitative 2D NMR. *Chem. Eur. J.* **2011,** *17*, 9529-9535.
71. Ma, R.; Xu, Y.; Zhang, X., Catalytic Oxidation of Biorefinery Lignin to Value-Added Chemicals to Support Sustainable Biofuel Production. *ChemSusChem* **2015,** *8*, 24-51.
72. Robert, D. R.; Bardet, M.; Gellerstedt, G.; Lindfors, E. L., Structural Changes in Lignin During Kraft Cooking Part 3. On the Structure of Dissolved Lignins. *J. Wood Chem. Technol.* **1984,** *4*, 239-263.
73. Petachem. http://www.petachem.com. (accessed November 11, 2016).
74. Ufimtsev, I. S.; Martinez, T. J., Quantum Chemistry on Graphical Processing Units. 3. Analytical Energy Gradients, Geometry Optimization, and First Principles Molecular Dynamics. *J. Chem. Theory Comput.* **2009,** *5*, 2619-2628.
75. Rohrdanz, M. A.; Martins, K. M.; Herbert, J. M., A Long-Range-Corrected Density Functional That Performs Well for Both Ground-State Properties and Time-Dependent Density Functional Theory Excitation Energies, Including Charge-Transfer Excited States. *J. Chem. Phys.* **2009,** *130*, 054112.
76. Saunders, V. R.; Hillier, I. H., Level-Shifting Method for Converging Closed Shell Hartree-Fock Wave-Functions. *Int. J. Quantum Chem.* **1973,** *7*, 699-705.
77. Kästner, J.; Carr, J. M.; Keal, T. W.; Thiel, W.; Wander, A.; Sherwood, P., DL-FIND: An Open-Source Geometry Optimizer for Atomistic Simulations†. *J. Phys. Chem. A* **2009,** *113*, 11856-11865.
78. Wang, L.-P.; McGibbon, R. T.; Pande, V. S.; Martínez, T. J., Automated Discovery and Refinement of Reactive Molecular Dynamics Pathways. *J. Chem. Theory Comput.* **2016,** *12*, 638-649.

79. Henkelman, G.; Uberuaga, B. P.; Jónsson, H., A Climbing Image Nudged Elastic Band Method for Finding Saddle Points and Minimum Energy Paths. *J. Chem. Phys.* **2000,** *113*, 9901-9904.
80. Henkelman, G.; Jónsson, H., Improved Tangent Estimate in the Nudged Elastic Band Method for Finding Minimum Energy Paths and Saddle Points. *J. Chem. Phys.* **2000,** *113*, 9978-9985.
81. E. D. Glendening, J., K. Badenhoop, A. E. Reed, J. E. Carpenter, J. A. Bohmann, C. M. Morales, C. R. Landis, and F. Weinhold, NBO, Version 6.0. 2013.
82. Younker, J. M.; Beste, A.; Buchanan, A., Computational Study of Bond Dissociation Enthalpies for Lignin Model Compounds: β-5 Arylcoumaran. *Chem. Phys. Lett.* **2012,** *545*, 100-106.
83. Blanksby, S. J.; Ellison, G. B., Bond Dissociation Energies of Organic Molecules. *Acc. Chem. Res.* **2003,** *36*, 255-263.
84. Sangha, A. K.; Parks, J. M.; Standaert, R. F.; Ziebell, A.; Davis, M.; Smith, J. C., Radical Coupling Reactions in Lignin Synthesis: A Density Functional Theory Study. *J. Phys. Chem. B* **2012,** *116*, 4760-4768.
85. van Scheppingen, W.; Dorrestijn, E.; Arends, I.; Mulder, P.; Korth, H.-G., Carbon−Oxygen Bond Strength in Diphenyl Ether and Phenyl Vinyl Ether: An Experimental and Computational Study. *J. Phys. Chem. A* **1997,** *101*, 5404-5411.

TOC Graphic